Microphase Separation of Diblock Copolymer Brushes in Selective Solvents: Single-Chain-in-Mean-Field Simulations and Integral Geometry Analysis

Jiafang Wang* and Marcus Müller

Institut für Theoretische Physik, Georg-August Universität, D-37077 Göttingen, Germany

Received November 19, 2008; Revised Manuscript Received January 8, 2009

ABSTRACT: Microphase separation of A-*b*-B diblock copolymer brushes in selective solvents is investigated by single-chain-in-mean-field (SCMF) simulations. Depending on the solvent selectivity of the blocks, the fraction (f) of the A block, and the grafting density (σ), perpendicular segregation, lateral segregation, or their combination occurs. Using extensive simulations, we obtain morphology diagrams in terms of f and σ for block copolymer brushes in different solvents. The morphologies of nanoscopic domains lack long-range order, and they are analyzed using integral geometry techniques.

I. Introduction

Grafting polymer chains onto a substrate to form polymer brushes is a versatile way to fabricate surface coatings, which can be applied in diverse areas such as colloidal stabilization,[1] drug delivery,[2] and tailoring adhesion or wettability.[3,4] Of special interest are brushes that consist of two or more immiscible components, which exhibit phase separation on nanoscopic length scales.[5−7] Block copolymer brushes and mixed homopolymer brushes are two typical examples.[8−11] The interplay between molecular architecture, irreversible grafting, and geometrical constraints due to the substrate gives rise to a variety of morphologies. Because the spatial structure is dictated by a subtle interplay between bonded and nonbonded interactions and conformational entropy, the free energy difference between different structures is only a small fraction of the thermal energy, k_BT, per molecule, and the spatial arrangement of the nanoscopic domains can be controlled by changing the macromolecular characteristics (e.g., chemical nature of the monomeric units, molecular architecture, grafting density) or the external environments (e.g., temperature, solvent properties).

The latter property is exploited to fabricate smart materials that respond to external stimuli, and it opens opportunities for a variety of applications. For instance, the wettability of a surface can be reversibly switched by controlling the average composition of the top of the brush. Experiments have demonstrated that this can be achieved by exposing mixed homopolymer brushes to different solvents.[8,9,12] The details of the lateral structure are less important for this application because a droplet of water is much larger than the typical size of the laterally phase-separated morphology; therefore, details of the structure will be averaged out. However, if one aims at tailoring the adsorption of proteins from solution, it is not the average composition of the top of the brush that is the relevant property but the small hydrophobic patches at the top, whose lateral dimensions are comparable to the size of the solute, that will already give rise to a significant adsorption.[13] Moreover, the reversible change of the lateral structure of the brush's top can be utilized to impart motion on adsorbed nano-objects.[14,15] This type of application relies on the ability to generate different, uncorrelated, laterally segregated surface patterns upon subsequent solvent-switching cycles, a property that is quantified by the domain memory measure.[16,17] This feature is dictated by fluctuations of the density (and composition) of the grafting points, which are strongly amplified by the structure formation in the multicomponent brush.[18]

The morphology of idealized block copolymer brush systems has been studied by weak-segregation calculations, scaling considerations, and self-consistent field theory.[19−27] The comparison between theoretical work and experiments shows that the theory reflects most features of self-assembly of block copolymer brushes exposed to selective solvents. The variety of pertinent properties ranging from the average composition of the brush's top to correlation effects between grafting point fluctuations and morphology, the subtle interplay of the immiscibility between blocks and solvent selectivity, and the vast selection of block copolymers and solvents for fabricating smart coatings require a numerical description. Some progress has been made in this direction.[18,28−30] Recently, Yin and coworkers[29] performed lattice Monte Carlo simulations to study the morphologies of block copolymer brushes in a selective solvent, and systematically investigated effects of the length of one block keeping the length of the other block constant. In our simulation study, we also utilize a coarse-grained representation that incorporates only the relevant interactions of the compressible mixtures of two distinct monomeric units. The solvent degrees of freedom are integrated out, and the effective interactions between monomeric units are described by a third-order free-energy functional. This coarse-grained model allows us to investigate the structure formation on the length scale of several domain sizes efficiently, to study correlations between morphologies that self-assemble on identical sets of grafting points, and to explore the influence of composition, grafting density, and solvent selectivity. The parameters of the free energy functional are inspired by a mixture of poly(acrylic acid) (PAA) and polystyrene (PS) in different solvents: dimethylformamide (DMF), methyl ethyl ketone (MEK), and water. This approach is only a first step toward a realistic modeling of nonbonded interactions, but it suffices to capture the six types of qualitatively different phase diagrams[31] that may occur in compressible mixtures according to the classification of Van Konynenburg and Scott.[32] Because of the lack of comprehensive thermodynamic data about the equation of the state of the PAA/PS/solvent mixture, a more quantitative approach is not warranted.

In this Article, we systematically study microphase separation of diblock copolymer brushes in various solvents using single-chain-in-mean-field (SCMF) simulation. This particle-based simulation scheme allows us to investigate the structure formation in large, 3D systems. Effects of solvent selectivity on microphase separation of diblock copolymer brushes are inves-

* Corresponding author. E-mail: wang@theorie.physik.uni-goettingen.de.

10.1021/ma8026047 CCC: $40.75
Published on Web 02/19/2009

tigated by constructing a diagram of morphologies in terms of the ratio of block lengths and the grafting density in various solvents. Our simulation results are placed in the context of alternative theoretical approaches and experiments. Because of the pronounced correlations between fluctuations of the grafting points and the morphology of the diblock-copolymer brush, the morphologies lack long-range order, and the variation of the morphology in response to the control parameters is completely gradual and occurs without thermodynamic singularities. To quantify the differences between the disordered structures, we analyze the lateral pattern of segregated domains using 2D Minkowski measures.

Our manuscript is arranged as follows: In the next section, we describe our coarse-grained model and provide details of the simulation technique. In the subsequent section, we discuss the morphology diagrams for different solvent qualities. A detailed analysis of the changes in the morphologies using Minkowski measures is presented in the fourth section. The manuscript closes with a brief summary and discussion.

II. Model and Simulation Method

We study microphase separation of A-*b*-B diblock copolymer brushes in solvents using SCMF simulations of a coarse-grained model. The grafting substrate is modeled as a nonpenetrable, hard wall at $z = 0$ without any preference for species A, B, or solvent. We consider a system with a lateral area $L \times L$. Periodic boundary conditions are applied in the lateral directions. The system is composed of n block copolymer chains, and $\sigma = n/L^2$ denotes the grafting density. The dimension of the system in the z direction, L_z, is much larger than the brush height, and a hard-wall boundary condition is applied at $z = L_z$.

In our coarse-grained model, the molecular architecture is described by a discretized Edwards Hamiltonian

$$\frac{\mathscr{H}_b[\{\mathbf{r}_i(s)\}]}{k_BT} = \prod_{i=1}^{n}\sum_{s=1}^{N-1}\frac{3(N-1)}{2R_{eo}^2}[\mathbf{r}_i(s) - \mathbf{r}_i(s+1)]^2 \qquad (1)$$

where N denotes the number of segments (or coarse-grained interaction centers) along the chain contour, and $\mathbf{r}_i(s)$ specifies the position of the s^{th} segment of the i^{th} polymer. The mean-square end-to-end distance, $R_{eo}^2 = \langle[\mathbf{r}_i(s=1) - \mathbf{r}_i(s=N)]^2\rangle_b$, of molecules subjected to only $\mathscr{H}_b$ is the only characteristic of the noninteracting polymers in the melt, and it sets the length scale. $N_A = fN$ segments are of species A, whereas $N_B = N - N_A$ segments belong to the B block of the copolymer. R_{eo} and f completely specify the architecture of the linear, flexible diblock copolymer. To form a brush, one end of each molecule is irreversibly grafted to a random position on the substrate. The lateral system size is $L = 16R_{eo}$, which exceeds the characteristic length scale of the phase-separated morphology by about a factor of 8. Therefore, finite-size effects due to a mismatch between the domain size and the finite extension of the simulation cell are negligible.

In addition to the connectivity of the macromolecules, relevant nonbonded interactions, $\mathscr{H}_{nb}$, are considered in the framework of a local density functional. The solvent is not treated explicitly. Rather than dealing with a nearly incompressible mixture of segment species A, segment species B, and solvent, we regard a compressible mixture of A and B segments, which interact via effective potentials. Formally, these potentials can be obtained by integrating out the degrees of freedom of the solvent particles. This decimation of the solvent degrees of freedom as well as the coarse graining of the bonded interactions that is the basis of the coarse-grained description of the molecular structure via the discretized Edwards Hamiltonian give rise to solvent-mediated interactions that are state-dependent and nonpairwise; that is, $\mathscr{H}_{nb}$ is a free energy rather than an interaction energy. In the following, we use the simplest form, a third-order expansion of the equation-of-state (EOS), that is capable of describing the qualitative features of the phase diagram of binary compressible mixtures

$$\frac{\mathscr{H}_{nb}[\hat{\rho}_A(\mathbf{r}), \hat{\rho}_B(\mathbf{r})]}{k_BT} = \int_V \frac{d^3\mathbf{r}}{R_{eo}^3}\left(\frac{1}{2}\sum_{\alpha,\beta=A,B}\upsilon_{\alpha\beta}\hat{\rho}_\alpha\hat{\rho}_\beta + \frac{1}{3}\sum_{\alpha,\beta,\gamma=A,B}w_{\alpha\beta\gamma}\hat{\rho}_\alpha\hat{\rho}_\beta\hat{\rho}_\gamma\right) \qquad (2)$$

$\hat{\rho}_\alpha(\mathbf{r})$ is the local number density of polymer species α in a volume R_{eo}^3. Note that the dimensionless density $\hat{\rho}_\alpha$ adopts large values in experimental systems. For instance, for a PAA molecule of molecular weight 27 kg/mol and end-to-end distance $R_{eo} = 10.6$ nm, a mass density of 1 g/cm$^3 \approx 1.2 \times 10^{-21}$kg/$R_{eo}^3$ corresponds to $\hat{\rho}_A \approx 27$.

We calculate $\hat{\rho}_\alpha(\mathbf{r})$ from the explicit molecular conformations

$$\hat{\rho}_\alpha(\mathbf{r}) = \frac{R_{eo}^3}{N}\sum_{i=1}^{n}\sum_{s=1}^{N}\gamma_\alpha(s)\delta(\mathbf{r} - \mathbf{r}_i(s)) \qquad (3)$$

where $\gamma_\alpha(s) = 1$ if the s^{th} segment is of type α (with $\alpha = A$ or B), and $\gamma_\alpha(s) = 0$ otherwise.[33] Straightforwardly, the density functional, eq 2, could be generalized to higher orders in the local density and would be able to parametrize sophisticated equations of states. Because of the lack of thermodynamic data about the system PAA/PS/solvent, however, we restrict ourselves in the following to the simple form of eq 2.

Whereas the form of $\mathscr{H}_{nb}$ is similar to a third-order virial expansion, we note that the coefficients, $\upsilon_{\alpha\beta}$ and $w_{\alpha\beta\gamma}$, are not obtained via a low-density expansion but were extracted from fitting the equation of state over the entire regime of relevant densities inside the brush,[31] which includes meltlike values. For a compressible binary system, there are three second-order coefficients and four third-order coefficients. The coefficients of the pure components, $\upsilon_{\alpha\alpha}$ and $w_{\alpha\alpha\alpha}$, have a transparent meaning: In a homogeneous, one-component bulk system, the pressure, p, takes the form

$$\frac{pR_{eo}^3}{k_BT} = \hat{\rho}_\alpha + \frac{\upsilon_{\alpha\alpha}}{2}\hat{\rho}_\alpha^2 + \frac{2w_{\alpha\alpha\alpha}}{3}\hat{\rho}_\alpha^3 \qquad (4)$$

The second-order terms reflect the quality of the solvent. A positive Fixmann parameter, $\upsilon_{\alpha\alpha} > 0$, describes a good solvent in which segments interact via a repulsive pairwise potential. Negative values of $\upsilon_{\alpha\alpha}$ correspond to a bad solvent, and they give rise to phase separation between a dense polymer melt and a solvent-rich phase. In this case, a positive third-order coefficient, $w_{\alpha\alpha\alpha} > 0$, is required for thermodynamic stability in the bulk. For sufficient segregation, the coexistence value of the pressure is vanishingly small, $p_{coex} \approx 0$, and the coexistence density of the melt is dictated by $\rho_{coex} = -(3\upsilon_{\alpha\alpha})/(4w_{\alpha\alpha\alpha})$. The isothermal compressibility adopts the value $1/\kappa_T \equiv -V[(\partial p)/(\partial V)]|_T = (1 + \upsilon_{\alpha\alpha}\rho_{coex} + 2w_{\alpha\alpha\alpha}\rho_{coex}^2)\rho_{coex}/k_BT$. The mixed second-order coefficient, υ_{AB}, characterizes the incompatibility between the A and B polymer species and is related to the Flory−Huggins parameter, χ.

The parameters of our free-energy functional are inspired by experiments on PAA-*b*-PS diblock copolymer brushes in various solvents, including DMF, MEK, and water. DMF is a cosolvent for PAA and PS blocks, and MEK is a good solvent for PS blocks but a bad solvent for PAA blocks. Water is a very bad solvent for PS blocks, and the solubility of PAA blocks in water can be adjusted by its pH value. Water is a bad solvent for PAA blocks at a low pH value and a good solvent at a high pH value. PAA and PS blocks are immiscible. In the following, we denote segments of the PAA block by species A and PS-monomeric repeat units by species B. Four different parameter

Table 1. Interaction Parameters for the Model Systems

solvent	SA	SB	SC	SD
v_{AA}	0.325275	−2.79721	4.62845	−9.2569
v_{BB}	0.258649	0.173237	−11.0412	−11.0412
v_{AB}	2.07856	0.638477	−2.33879	−8.52973
w_{AAA}	0.212006	1.0418	0	3.87862
w_{BBB}	0.150328	0.141527	3.66696	3.66696
w_{AAB}	0.189051	0.535554	0	3.80674
w_{ABB}	0.168581	0.27531	0	3.7362

sets are employed to mimic the behavior in DMF (solvent SA), MEK (solvent SB), and water at high pH value (solvent SC) and low pH value (solvent SD), respectively. The coefficients of the free-energy functional for these polymer−solvent mixtures are compiled in Table 1. The second-order coefficients are calculated from Flory−Huggins parameters for cases in which experimental data are available,[34,35] and they otherwise qualitatively reflect the solvent quality.[36] The third-order coefficients have been adjusted to limit the maximal local density.

In our numerical implementation, we use a fine collocation grid with spacing, ΔL, to calculate the densities at a grid vertex, $\mathbf{c}$, from the explicit particle coordinates according to

$$\hat{\rho}_\alpha(\mathbf{c}) = \frac{R_{eo}^3}{N\Delta L^3}\sum_{i=1}^{n}\sum_{s=1}^{N}\Pi(\mathbf{r}_i(s),\mathbf{c})\gamma_\alpha(s) \tag{5}$$

where $\Pi(\mathbf{r}, \mathbf{c})$ is a linear assignment of the segment position, $\mathbf{r}$, onto the point $\mathbf{c}$ of the collocation grid[37−39]

$$\Pi(\mathbf{r},\mathbf{c}) = \prod_{\alpha=x,y,z}\left(1-\frac{|\mathbf{r}_\alpha-\mathbf{c}_\alpha|}{\Delta L}\right) \tag{6}$$

if the distance between the grid point and the segment position along each Cartesian direction is less than ΔL and $\Pi(\mathbf{r}, \mathbf{c}) = 0$ otherwise. ΔL characterizes the spatial range of interactions, and it is chosen to be of the same order as the typical distance, $/R_{eo}\sqrt{N}$, between bonded segments. Similar schemes are used for particle-in-cell techniques in plasma physics[40] or particle-mesh methods in electrostatics[41,42] to assign a particle-based density or charge distribution onto a lattice. The spatial integral in eq 2 is evaluated via the collocation grid

$$\frac{\mathscr{H}_{nb}[\hat{\rho}_A,\hat{\rho}_B]}{k_BT} = \frac{\Delta L^3}{R_{eo}^3}\sum_{\mathbf{c}}\left(\frac{1}{2}\sum_{\alpha,\beta=A,B}v_{\alpha\beta}\hat{\rho}_\alpha\hat{\rho}_\beta+\frac{1}{3}\sum_{\alpha,\beta,\gamma=A,B}w_{\alpha\beta\gamma}\hat{\rho}_\alpha\hat{\rho}_\beta\hat{\rho}_\gamma\right) \tag{7}$$

The partition function in the canonical ensemble can be expressed as

$$Z \approx \int \mathscr{D}\{\mathbf{r}_i(s)\}\,\exp\left(-\frac{\mathscr{H}_b[\{\mathbf{r}_i(s)\}]+\mathscr{H}_{nb}[\hat{\rho}_A,\hat{\rho}_B]}{k_BT}\right) \tag{8}$$

where $\mathscr{D}\{\mathbf{r}_i(s)\} = \prod_{i=1}^{n}\prod_{s=1}^{N} d^3\mathbf{r}_i(s)$ is the element of configurational integral and the densities $\hat{\rho}_A$ and $\hat{\rho}_B$ are functions of the explicit particle coordinates. In SCMF simulations,[43,44] the nonbonded interactions, $\mathscr{H}_{nb}$, between molecules are replaced by real fluctuating background fields that mimic the interactions of a segment with its instantaneous environment. This approximation results in a decoupling of the molecules, and the ensemble of independent molecules can be efficiently simulated on a parallel computer. To capture the spatial and temporal fluctuations of these interactions, the background fields have to be frequently calculated from the instantaneous density distribution. The background field, $\hat{w}_A$, that acts on an A polymer is given by

$$\hat{w}_A(\mathbf{c}) = \frac{R_{eo}^3}{\Delta L^3}\frac{\partial}{\partial\rho_A(\mathbf{c})}\frac{\mathscr{H}_{nb}}{k_BT} \tag{9}$$

and a similar expression holds for $\hat{w}_B(\mathbf{c})$. During the updating of the molecular conformations by an SCMF simulation, nonbonded interactions are approximated by fixed background fields. This replacement yields

$$\frac{\mathscr{H}_{nb}^{SCMF}[\hat{\rho}_A,\hat{\rho}_B]}{k_BT} = \frac{\Delta L^3}{R_{eo}^3}\sum_{\mathbf{c}}[w_A(\mathbf{c})\hat{\rho}_A(\mathbf{c})+w_B(\mathbf{c})\hat{\rho}_B(\mathbf{c})] \tag{10}$$

SCMF simulations consist of cycles during which (1) the explicit molecular conformations in the external fields evolve independently from each other via a MC simulation for a short predetermined number of MC steps (MCS), and (2) the background fields are updated after each MCS according to eq 9. Then, the MC cycle commences again. We use smart Monte Carlo moves[46,47] in the first part of the cycle, where the trial displacements of the segments are constructed from the forces. For the chain discretization, $N = 32$, a single chain in the bulk diffuses a distance of the order $R_{eo} = \sqrt{6Dt}$ (D being the self-diffusion coefficient) in $t = 1500$ MCS.

Whereas the chains are decoupled during the Monte Carlo simulation of the ensemble of independent molecules in the background fields, by frequently updating the fields, we approximately restore the correlations between molecules. The quality of this quasi-instantaneous field approximation is controlled by both the coarse-grained parameters and the discretization of the molecular contour, N, and space, ΔL. In previous work,[45] we demonstrated that in dense systems with a fine contour discretization, N, and a frequent update of the background fields, the quasi-instantaneous field approximation is excellent.

Our simulations start with a disordered configuration of block copolymer brushes with a random pattern of grafting points. To equilibrate the morphology, we gradually reduce the temperature according to the scheme (simulated annealing) $T_j = kT_{j-1}$, where T_j is the temperature at the j^{th} annealing step and k is a factor controlling the rate of temperature decrease. In our simulations, we set each annealing step to last 7000 MCS and $k = 0.9$; it takes 60 cooling steps to reach the final temperature, after which an additional 70 000 MCS are used to obtain the final morphologies at 490 000 MCS. Longer annealing steps and slower temperature decrease have been used to verify equilibration.

III. Simulation Results

For the results presented here, the chain discretization of block copolymer is set to $N = 32$. This number is sufficient for representing the Gaussian architecture of flexible macromolecules. B-*b*-A is used to denote block copolymer brushes grafted by B ends, and these brushes differ from A-*b*-B systems, which are grafted by A blocks. We study the morphologies in the different solvents. For each solvent, A-*b*-B and B-*b*-A block copolymer brushes are investigated by varying the relative block length, f, and the grafting density, σ.

A. Cosolvent (SA) and Weakly Selective Solvent (SB). Solvent SA (modeling DMF) is a marginally good solvent for both A and B blocks. Both blocks are swollen by the solvent, but the solvent exhibits a slight preference for the A block. The swelling reduces the effective incompatibility between A and B blocks. In this solvent, the morphologies of A-*b*-B brushes are very similar to those of B-*b*-A brushes. Therefore, we present only the results of A-*b*-B copolymer brushes. Figure 1 illustrates the different morphologies for $\sigma R_{eo}^2 = 50$ and various values of composition, f. Figure 2 presents the laterally averaged profiles of the dimensionless density, $\hat{\rho}$, as a function of the distance, z, from the grafting substrate.

For tethered diblock copolymers, there is a natural asymmetry in the distribution of segments perpendicular to the grafting substrate; that is, segments that belong to the grafted block are preferentially located close to the substrate, whereas the other

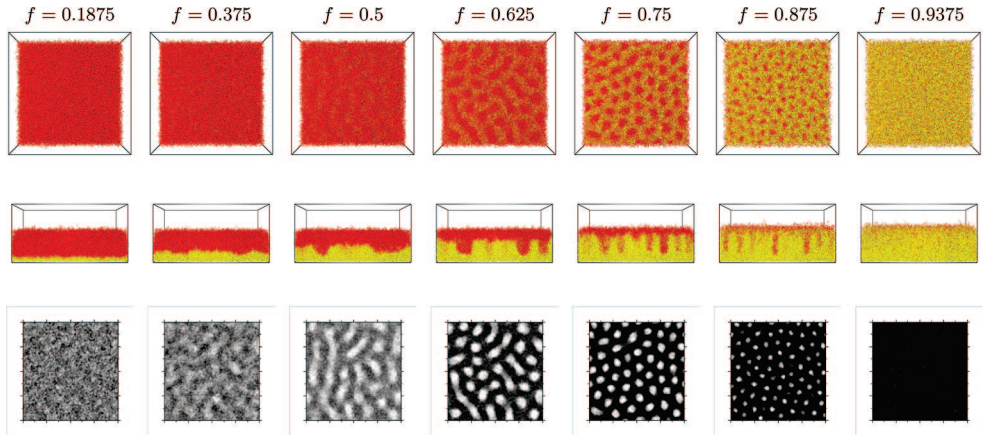

Figure 1. Illustration of morphologies of diblock copolymer A-*b*-B brushes in cosolvent SA for grafting density $\sigma R_{eo}^2 = 50$ and various values of fraction, f, of the A block, as indicated in the key. The top and side views are compiled in the first and second row, and the corresponding maps for $\sum_z \rho^-(x, y) = \sum_z (\hat{\rho}_B - \hat{\rho}_A)$ are given in the bottom row.

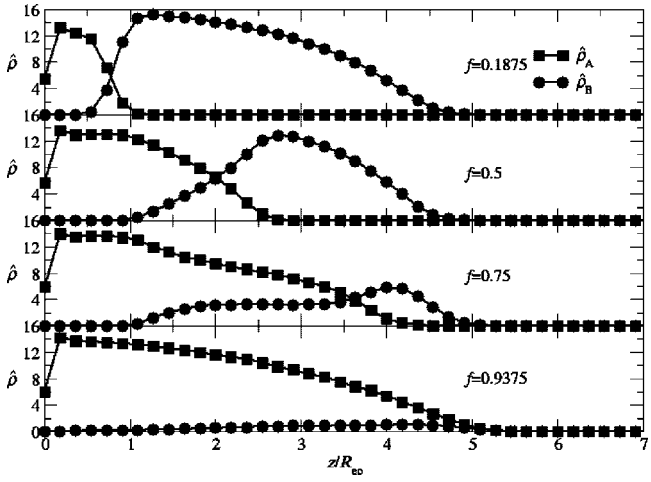

Figure 2. Laterally averaged density profiles as a function of the distance, z, perpendicular to the grafting surface for A-*b*-B diblock brushes with grafting density $\sigma R_{eo}^2 = 50$ in solvent SA. The different panels present various values of fraction, f, of the A block, as indicated in the key.

segment species is enriched at the brush's top. This perpendicular segregation tendency is enhanced by the incompatibility of the two species because the segregation decreases the number of unfavorable A/B contacts. Our simulation results show that perpendicular segregation is one possibility, but lateral segregation does occur under specific conditions.

For very strong asymmetries, $f \lesssim 0.1$ or $f \gtrsim 0.95$, there is no noticeable segregation. The distribution of the minority component is laterally homogeneous, and the concentration profile perpendicular to the grafting surface indicates a broad distribution with the grafted component A being enriched at the bottom and the nongrafted component being preferentially located on the top. In the following, we denote this structure to be disordered.

As the fraction, f, of the bottom A block increases, a layer of A forms at the grafting surface, which is separated by a well-defined interface from a B domain at the top. Note that in a bulk melt of diblock copolymers with comparable composition one would observe micelles of the minority component that would crystallize onto a body-centered cubic (BCC) lattice. The difference between tethered and bulk block copolymers can be ascribed to the serious constraints that the grafting imposes on the short bottom blocks, preventing them from assembling into spherical or cylindrical domains.

This "sandwich" structure of the copolymer brush is gradually formed as we increase f, and it does not involve lateral structure formation; that is, the A/B interface runs parallel to the grafting substrate and exhibits only minor fluctuations of the local interface position. These fluctuations are small in amplitude and are of short wavelengths (cf. morphology of the A-*b*-B diblock brush with $f = 0.1875$ in solvent SA shown in Figure 1). They arise from quenched fluctuations of the density of grafting points and thermal fluctuations. The latter contribution resembles capillary waves, which are strongly constrained because of the coupling of the local interface position with the grafting surface. There is, however, no specific lateral wave vector singled out that would indicate a characteristic length scale of a lateral morphology. The well-developed interface between the A domain at the grafting substrate and the B domain on the top surface also is clearly observable in the 1D density profiles perpendicular to the substrate (cf. Figure 2), which show that there is little interdigitation between A and B blocks.

Upon further increasing f, we observe that the A/B interface moves farther away from the grafting substrate. The constraints that limit the thermal fluctuations of the A/B interface become weaker as the length of the bottom A block increases and the A/B interface become rougher. These interface fluctuations give rise to a rather broad interface in the laterally averaged 1D profiles of Figure 2. Although perpendicular segregation is dominant, there are pronounced lateral fluctuations, which can be visualized by the 2D composition map, $\sum_z \rho^-(x, y) \equiv \sum_z (\hat{\rho}_B - \hat{\rho}_A)$, depicted in the bottom row of Figure 1. We observe that the contrast of these maps increases with f quantifying the growth of the amplitude of interface fluctuations.

As we further increase f, the fluctuations of the A/B interface become strong, and lateral structures can be clearly identified in lateral composition maps $\sum_z \rho^-(x, y)$, which are obtained by integrating over the direction perpendicular to the grafting substrate. For $0.4 \lesssim f \lesssim 0.65$, the lateral structure in the local position of the A/B interface adopts elongated, wormlike shapes. We denote this structure to be a ripple structure because the domains do not exhibit long-range order, unlike its counterpart in thin films of (nongrafted) diblock copolymers. Increasing f, we observe that the aspect ratio of lateral domains gradually decreases. For $0.7 \lesssim f \lesssim 0.9$, the lateral structure becomes more disklike, and there is an overt tendency to hexagonally arrange these circular domains, but no long-range order is established. In the following, we denote this morphology to be a "dimple" structure. At the same time, the thickness of the A layer at the bottom increases, and that of the B layer at the top decreases. The excursions of the A/B interfaces approach the top surface, and eventually, the thin top B layer begins to break up (cf. the

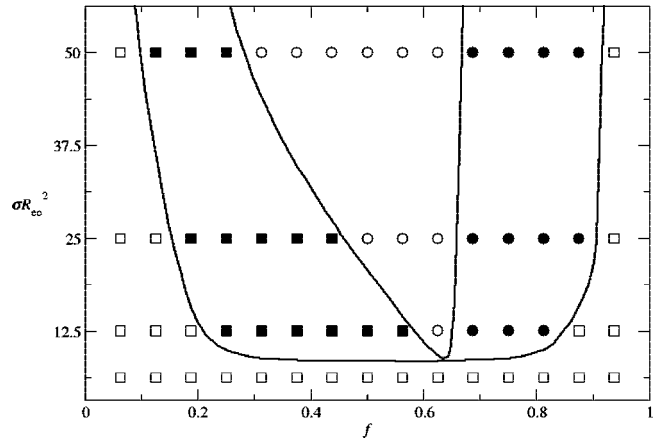

Figure 3. Diagram showing morphologies of A-*b*-B diblock brushes in solvent SA as a function of the fraction, *f*, of the A block and the grafting density, σR_{eo}^2: disordered structures without obvious segregation (□), "sandwich" structures showing vertical segregation but no obvious lateral heterogeneity (■), and structures exhibiting lateral patterns (● for dimple structures and ○ for ripple structures).

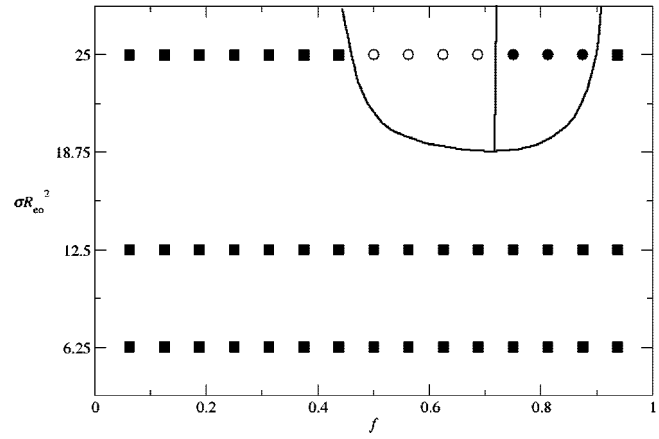

Figure 4. Diagram showing morphologies of A-*b*-B diblock brushes in solvent SB as a function of the fraction of the *A* block, *f*, and the grafting density, σR_{eo}^2: "sandwich" structures showing vertical segregation but no obvious lateral heterogeneity (■) and structures exhibiting lateral patterns (● for dimple structures and ○ for ripple structures).

configuration snapshot of $f = 0.875$ in Figure 1). As a consequence of strong excursions in the A/B interface, the laterally averaged 1D profiles as a function of the distance from the grafting substrate become very broad (see profiles for $f = 0.75$ in Figure 2), and they should not be mistaken for characterizing the profiles across a domain boundary.

For larger compositional asymmetries, the lateral extension of the B dimples decreases, and eventually, one encounters a disordered structure for extreme values of *f* (cf. data for $f = 0.9375$ in Figure 1). The broadening of the 1D profiles for this extreme composition chiefly stems from the reduced incompatibility as the density of the minority component becomes very small.

Interestingly, the lateral structure formation and perpendicular segregation are strongly coupled. There always remains a thin enrichment layer of the B component at the top of the brush. The enrichment stems from the grafting of the A block, and the preference of the solvent for the A component is not strong enough to counteract. This surface segregation, in turn, would result in a slight relative depletion of B at the center of the brush. This effect, however, is overcompensated by the natural stratification of the composition perpendicular to the grafting substrate (i.e., the exclusion of B from the vicinity of the grafting substrate), which results in an increase in the B species at the center. Therefore, the sequence of phases is not symmetric around $f = 1/2$ but is slightly screwed toward larger *f* values. Moreover, the sandwich structure occurs for only small values of *f*; for small amounts of the top block, however, we observe a change from a dimple structure to a disordered morphology. This asymmetry with respect to $f = 1/2$ becomes even more pronounced as the grafting density is decreased because the reduced stretching of the chains facilitates rearrangements perpendicular to the grafting substrate.

Figure 3 summarizes the different morphologies observed in the simulation as a function of the grafting density, σR_{eo}^2, and relative block length, *f*. As we decrease the grafting density, σ, not only the height of the brush but also the polymer density inside the brush layer decrease. Therefore, the repulsive interactions are diluted by the good solvent. This reduction in the effective incompatibility is the main effect of decreasing the grafting density. It can be clearly observed in the reduction of the segregation between the domains and the slightly smaller characteristic length scale of the lateral structure at lower values of σ. As the tendency for structure formation decreases, the stability of the sandwich structure increases relative to the dimple morphology. For $\sigma R_{eo}^2 < 6.25$, only disordered structures are observed in the simulations.

Qualitatively, the physical principles that underlie microphase separation of diblock copolymers in the bulk and structure formation in diblock copolymer brushes are similar. The structure is dictated by a balance between enthalpic interactions, which tend to minimize A/B contacts, and entropic contributions, which aim to minimize the distortion of the molecular conformations. There are, however, several important differences that arise from the constraint of immobile grafting of the diblock copolymers onto the grafting substrate: (i) The chain conformations of the disordered system are different. In a disordered diblock copolymer melt, the chain conformations are Gaussian, in the absence of a repulsion between A- and B-segment species, and there is no spatial variation of the average composition. In a disordered copolymer brush, the chain conformations stretch away from the grafting substrate to reduce the repulsive segmental interactions. Therefore, the chain's end-to-end vector has a well-defined orientation, and this would lead to a stratification of the composition perpendicular to the grafting substrate even if the components were perfectly miscible.[48] Therefore, the sequence of morphologies is not symmetric with respect to composition, but the sequence (disordered, sandwich, ripple, dimple, disordered) is observed as a function of the architecture, *f*, of the diblock copolymer. (ii) Unlike the morphologies of diblock copolymers in the bulk, the morphologies observed in diblock copolymer brushes lack long-range order. This absence of long-range order, which is clearly visible in Figure 1, is not due to insufficient relaxation in our simulations, but it is also observed in experiments. It stems from the quenched density fluctuations of the grafting points, the coupling between density and composition fluctuations in our compressible model, and the amplifications of these fluctuations by the structure formation in the microphase-separated brush. Therefore, the lines in the diagram of morphologies shown in Figure 3 should not be mistaken for the location of thermodynamic transitions between distinct phases, but they merely indicate the rather broad and gradual crossover between the different morphologies.

In solvent SB, which is slightly better for the B component than for the A component, qualitatively similar morphologies are observed. The crossovers between different morphologies are shifted, as shown in the morphology diagram Figure 4, indicating that even slight solvent selectivity affects the competition between lateral and perpendicular segregation. The stability of the sandwich structure is greatly improved if the

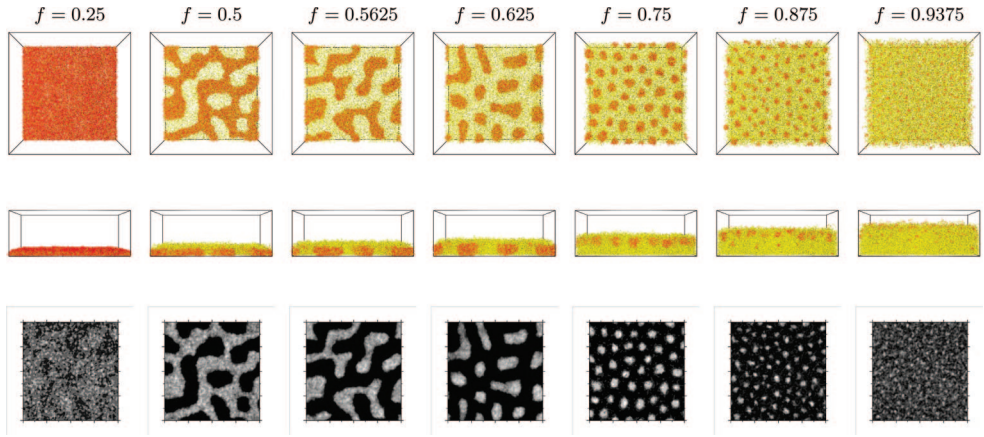

Figure 5. Illustration of morphologies of A-*b*-B diblock brushes in solvent SC for the grafting density $\sigma R_{eo}^2 = 12.5$ and various values of the fraction, *f*, of the A block. The top and side views are depicted in the first and second row, and the corresponding lateral maps of $\sum_z (\hat{\rho}_B + \hat{\rho}_A)$ are shown in the bottom row.

solvent prefers the nongrafted block, that is, A-*b*-B in solvent SB, and the relative stability of ripple structures increases with respect to the sandwich morphologies if the solvent is bad for the nongrafted block, that is, a B-*b*-A brush in solvent SB.

In experiments, nonselective solvents are utilized to "erase" lateral structures, and often, the surfaces of copolymer brushes in cosolvents appear to be smooth and featureless.[11,14] These experimental findings are in agreement with our simulation results. The main effect of the cosolvent is to swell the brush and thereby dilute the repulsive interactions between the different segment species. If the grafting density is very high, however, less solvent will enter the brush, and lateral structure formation may become observable. Additionally, longer grafted blocks and larger incompatibility between segment species will favor lateral phase separation. Few experiments report on lateral structure formation in copolymer brushes in cosolvents. Zhao and coworkers[11] observed ripple and dimple structures in polystyrene-*b*-poly(methyl acrylate) (PS-*b*-PMA) brushes in CH_2Cl_2 (good solvent for both PMA and PS) for composition $f \simeq 0.727$ and $f \simeq 0.806$, respectively. The authors hypothesized that the lateral segregation arises because of the large incompatibility between the segment species. In a polystyrene-*b*-poly(methyl methacrylate) (PS-*b*-PMMA) copolymer brush immersed in the same solvent, no lateral structures are experimentally observed, but the segment incompatibility is about two orders of magnitude lower than that in the PS-*b*-PMA system. Moreover, our simulations indicate that around $f = 0.65$, laterally segregated domains are buried below a thin B-rich layer on the top of the brush. Such structures may be difficult to detect in experiments that are sensitive to only the chemical composition of the topmost layer.

B. Highly Selective Solvent (SC). Solvent SC (modeling water at high pH value) is a good solvent for the A block and a poor solvent for the B block, and there is a large difference in solubilities between the components. A blocks are highly swollen, and B blocks are collapsed. The large incompatibility between B blocks and solvent SC results in a strong effective attraction between B blocks. Moreover, despite the immiscibility of A and B blocks (i.e., $\upsilon_{AB} - (\upsilon_{AA} + \upsilon_{BB})/2 > 0$), B domains prefer to be covered by A segments (i.e., $\upsilon_{AB} < 0$) to avoid the highly unfavorable SC/B contacts.

First, we consider A-*b*-B copolymer brushes where the solvophilic A blocks are grafted. Figure 5 presents the different morphologies observed in the simulations as a function of the copolymer composition, *f*, at intermediate grafting density, $\sigma R_{eo}^2 = 12.5$. Both snapshots of typical configurations viewed from the top and the side and 2D distributions of the composition

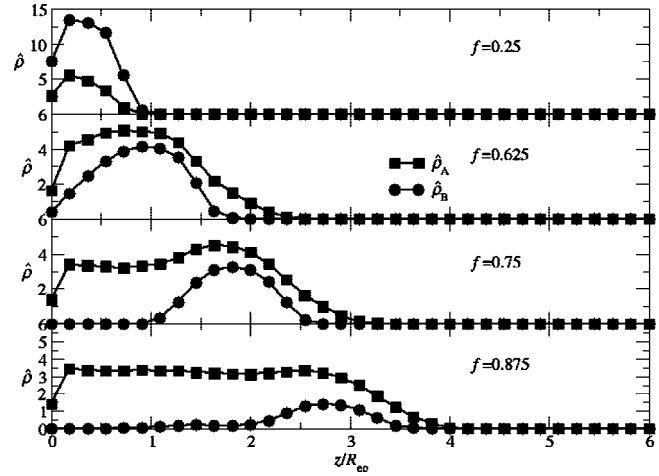

Figure 6. Laterally averaged density profiles along the perpendicular direction (*z*) for A-*b*-B diblock brushes in solvent SC for grafting density $\sigma R_{eo}^2 = 12.5$ and various values of fraction, *f*, of the A block.

integrated perpendicular to the grafting substrate $\sum_z \rho^+(x, y) \equiv \sum_z (\hat{\rho}_B + \hat{\rho}_A)$ are shown.

For small amounts of the solvophilic A block, we observe a collapsed B brush. In Figure 6, we present the corresponding laterally averaged profiles of the densities as a function of the distance, *z*, from the grafting substrate. These data indicate that the A component is rather uniformly dispersed in the collapsed B brush.

As the relative length of the solvophilic grafted A block increases, the collapsed B layer breaks up, and the holes of the perforated layer are enriched with A. Upon further increasing the fraction, *f*, of A segments, two phenomena occur: (i) The shape of the A domains changes from dimple structure to ripple structure; eventually, for very large values of *f*, ripples and dimples of the B component are formed. The latter structures resemble surface-attached wormlike and spherical micelles that the nongrafted amphiphiles would form in solvent SC. The grafted A block stretches, tilts, and wraps around the B domains to shield them from the poor solvent ("onion" structure).[21] (ii) For small *f*, the short A block ties the B domains down to the substrate. This pinning is further enhanced by the tendency of the short A block to coat the B domain and the enthalpic advantage of the B domain to make contact with the neutral grafting substrate rather than the hostile solvent. As the length of the grafted A block increases, however, the grafting and connectivity impose less serious constraints on the molecular

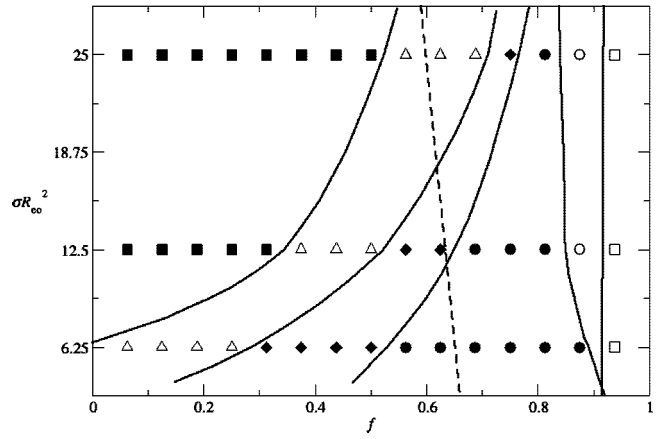

Figure 7. Morphology diagram of A-*b*-B diblock brushes in solvent SC as a function of the fraction of the A block, *f*, and the grafting density, σR_{eo}^2: perpendicularly segregated "sandwich" structure (■), perforated layer (△), nearly bicontinuous ripple structures (◆), dimple structure with spherical micelles on the same height (●), dimple structures with spherical micelles of diffusive distribution of heights (○), and nonaggregating chains (□). The dashed line represents the crossover from pinned structures at low *f* to unpinned structures at high *f*.

conformations, and the collapsed B domains becomes unpinned from the grafting substrate. The 1D density profiles reveal that for $f \lesssim 0.65$, the B domains sit on the grafting substrate, whereas for longer A blocks they are located in the top half of the brush, but they are still covered by a thin layer of A segments. Also the lateral arrangement of the B domains is less constrained at larger values of *f*; if they are unpinned from the substrate, then B domains on the top tend to arrange in a locally hexagonal pattern and also, the polydispersity of their sizes appears to be smaller.

As *f* further increases, the size of the B domains decreases, and the distance between the center of the B micelles and the grafting substrate exhibits a rather broad distribution, as can be observed in the 1D density profiles. At $f = 0.875$, even an indication of a rather diffusive distribution of micelle heights can be observed; larger micelles on the top of the brush and smaller B domains in the middle are visible in the snapshots presented in Figure 5. As *f* becomes very large, the B domains become very small, and the structure is dictated by the swollen A chains.

The diagram of the different morphologies as a function of the A fraction, *f*, and the grafting density, σ, is presented in Figure 7. At very low grafting density, even a pure B brush ($f = 0$) forms a perforated layer or dimples rather than collapsing into a laterally homogeneous layer. For slightly larger *f* and low grafting density, the analogy between the structures of a diblock copolymer brush and surface adsorbed micelles becomes very apparent, and the stretching and tilting of the individual A blocks can be clearly observed ("A legs"). The morphology of a brush resembles a dense array of wormlike or spherical micelles for intermediate and large values of *f*, respectively. To fabricate those laterally structured surfaces by the adsorption of micelles from the bulk, however, one would have to fine-tune the concentration of the amphiphiles in the bulk solution and the interactions at the substrate.[49] In the case of irreversibly grafted copolymers, those laterally structured layers are stable and form without tuning the interaction with the substrate.

Because the demarcation between the distinct morphologies depends on the grafting density, by changing σ, we can induce crossovers between different structures. A larger grafting density favors larger domains of B. For instance, by increasing the grafting density, σ, at $f = 0.6$, we observe the sequence of pinned spherical micelles, wormlike micelles, and a perforated layer of B blocks coated by the grafted component. The increase in the grafting density may also lead to an unpinning of the collapsed B domains from the grafting substrate to the upper half of the brush.

Our results indicate that unless the bottom A blocks are very short, the collapsed B domains are immersed in swollen A blocks. Therefore, after the removal of the solvent, the topmost surface will be covered by the A component. Such brushes show strong solvent responsiveness with respect to changing solvents in agreement with experiments.[10,11] To shield the collapsed B domains from the solvent, block copolymers have to adopt back-folding conformations, which reduces the conformational entropy. Adjusting the ratio of block length and the solvent selectivity, our simulations as well as those of Yin and coworkers[29] indicate the possibility of fabricating structures where the collapsed B domains are on the top of the brush.

Self-assembly of block copolymer brushes in selective solvents favoring the bottom block gives rise to a rich morphological behavior. Therefore, it has been studied experimentally,[10,11,14,50−56] theoretically,[20,21] and by simulations.[29,30] Our simulation results are in good agreement with previous theoretical and experimental results. For A-*b*-B diblock brushes in a selective solvent, which is marginally good for the grafted A block and poor for the B block, Zhulina and coworkers[20] have predicted by 2D self-consistent field calculations and scaling considerations that an increase in the insoluble B block leads to phase sequence from nonaggregated chains to spherical micelles (A-leg tethered micelles or pinned micelles with an A coating denoted as "onion" structure) and then to a perforated B layer. Yin and coworkers[29] also studied morphologies of diblock copolymer brushes in selective solvents favoring the bottom blocks using lattice Monte Carlo simulations. In their simulations, they investigated effects of the length of an individual block by fixing the length of the other block. They observed that one can induce morphological transitions from a continuous layer via a perforated layer, ripple structures, or wormlike micelles to spherical micelles by decreasing the length of top block or increasing the length of bottom block. These findings are corroborated by our results, noting that increasing the chain length of one component in their simulations corresponds to simultaneously decreasing the dimensionless grafting density, σR_{eo}^2, and increasing the fraction, *f*, of that block; that is, changing $N_{Ao} \rightarrow N_A$ at fixed N_{Bo} corresponds to $f = N_{Ao}/(N_{Ao} + N_{Bo}) \rightarrow N_{Ao}/(N_A + N_{Bo})$ and $\sigma_o R_{eo}^2 \rightarrow \sigma R_{eo}^2 = \sigma_o R_{eo}^2 (N_{Ao} + N_{Bo})/(N_A + N_{Bo})$. Given the location of crossovers in the diagram of morphologies, it appears that at the investigated grafting densities changing the length of the grafted A block is more efficient in inducing structural changes than varying the length of the top block.

Although our model is designed to mimic PAA-*b*-PS in water at a high pH value, our simulation results are consistent with experimental results in similar systems.[14,55,56] For poly(methyl methacrylate)-*b*-poly(glycidyl methacrylate) (PMMA-*b*-PGMA) brushes in solvent toluene and poly(benzyl-*n*-methacrylate)-*b*-polystyrene (PBnMA-*b*-PS) brushes in solvent acetone, where both solvents swell the bottom blocks and are poor solvents for the top blocks, Santer and Rühe[14] found morphological transitions from ripples, to wormlike micelles, to dimple structures by increasing the length of the bottom blocks while keeping the length of the top block constant. Xu and coworkers[55] observed that when the solvent is switched from water (favoring the top block) to hexane (favoring the bottom block), the solvent responsiveness of poly(*n*-butyl methacrylate)-*b*-poly(2-(*N*,*N*′-dimethylamino)ethyl methacrylate) (PBMA-*b*-PDMAEMA) brushes was suppressed by long top blocks but enhanced by the extension of the bottom blocks. This is in qualitative

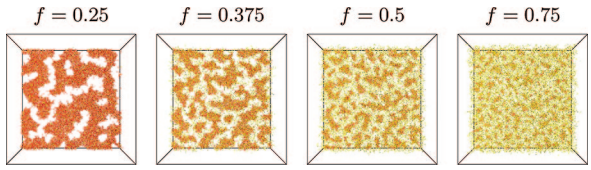

Figure 8. Illustration of morphologies (top views) of B-*b*-A diblock copolymer brushes in solvent SC for the grafting density $\sigma R_{eo}^2 = 6.25$ and various values of the fraction, f, of the A block.

agreement with our findings. For A-*b*-B block brushes with $\sigma R_{eo}^2 = 12.5$ and $f \lesssim 0.1875$, the topmost surface is entirely composed of the B component, which results in no response to a change in solvent quality. In the interval $0.1875 \lesssim f \lesssim 0.375$, both components occupy the upper part of the brush, which exhibits a weak response to solvent changes. At an even larger f, the bottom block is enriched at the brush surface, and those systems exhibit a very strong response to solvent stimuli. For poly(2-hydroxyethyl methacrylate)-*b*-poly(methyl methacrylate) (PHEMA-*b*-PMMA) brushes in solvent ethanol, which selectively collapses the top block, Tomlinson and Genzer found that the length of top PMMA blocks mainly determined the sizes of the collapsed domains, and the length of bottom PHEMA blocks mainly affected the lateral confinement.[56] This is corroborated by our simulations. For sufficiently long bottom blocks, the B domains resemble bulk micelles, and the size of the B-core scales, $R_{core} = 0.9\sqrt[6]{\chi N_B} R_{eoB}$ ($R_{eoB} \sim \sqrt{N_B}$ is the size of the B block),[57] is independent of the size of the A block.

The behavior of block copolymer brushes grafted with a solvophobic B block, B-*b*-A copolymer brushes, strongly differs from that of A-*b*-B copolymer brushes. Figure 8 presents some typical morphologies of B-*b*-A copolymer brushes in solvent SC. The bottom B blocks are collapsed, and the top blocks are swollen; that is, both the grafting constraint and the solvent selectivity favor a sandwich structure. Because the B block is located at the substrate, it is shielded from the unfavorable solvent interactions from the bottom. The swollen A blocks, in turn, shield the B domain from solvent contacts at the top and simultaneously extend into the solvent.

When N_A is small, the short A blocks are located inside the collapsed B domain. For larger values of N_A, additional A blocks cover the B domain and extend in solvent. The grafted B blocks form a continuous layer at high grafting density and large values of N_B. Upon decreasing one of these characteristics, σ or N_B, we observe that this B layer breaks up into a perforated layer, a nearly bicontinuous ripple phase with elongated domains, and a dimple phase with disklike domains. This behavior strongly resembles the behavior of a single-component brush in a bad solvent.[18,58−60] Such morphologies have flowerlike structures where the collapsed B blocks form cores and swollen A blocks shield them from unfavorable solvent contacts like "petals". Again, the size of cores primarily depends on N_B and the grafting density but is rather insensitive to N_A. These flowerlike micelles were also predicted by Zhulina and coworkers[21] in diblock copolymer brushes grafted by ends of insoluble blocks at low grafting densities. In our simulations, we demonstrate that by increasing the grafting density or the length of the B blocks, a morphological transition from isolated micelles with B cores to connected domains and then to a continuous B layer occurs. This is consistent with experimental reports by Xiong and coworkers in PS-*b*-PMMA treated by 2-methoxyethanol,[50] where they found that by increasing the grafting density the discrete domains started to overlap and a continuous layer formed.

C. Poor Solvent (SD). Solvent SD (modeling water at low pH value) is poor for both A and B blocks, with a small preference for the A block. Both blocks collapse in solvent SD, and their mutual incompatibility is less than the incompatibility between each individual component and the solvent. Therefore, A/B contacts are more favorable than contacts with the solvent. The effective attraction between A/B blocks is weaker than that between B/B blocks but stronger than the effective attraction between A/A blocks.

The typical morphologies of A-*b*-B brushes in solvent SD are depicted in Figure 9, and the structural properties observed in the simulations are summarized in the diagram of morphologies, Figure 10. At sufficiently high grafting densities and not-too-large compositional asymmetry, a sandwich structure forms that is composed of a bottom A layer and a collapsed B layer on top.

At a high grafting density $\sigma R_{eo}^2 = 12.5$ or $\sigma R_{eo}^2 = 25$, the collapsed block copolymers completely cover the substrate. By increasing f at $\sigma = 12.5$, the fraction of top B blocks decreases, and we observe a similar morphological sequence from continuous layers ($f \lesssim 0.4375$), to perforated layers ($0.5 \lesssim f \lesssim 0.65$), to ripple structures ($0.6875 \lesssim f \lesssim 0.85$), to dimples ($0.875 \lesssim f \lesssim 0.9$), and to unsegregated chains $f \gtrsim 0.92$. At different grafting density, a similar sequence is observed when increasing f, but the boundary between different morphologies will shift to lower values of f at a small grafting density and higher values of f at a large grafting density.

At a low grafting density, $\sigma R_{eo}^2 = 6.25$, there is not enough copolymer material to completely cover the substrate, and some lateral structure with voids emerges. The location of these voids correlates with fluctuations in the grafting density. At small values of f, some A blocks are buried under collapsed B domains, and other A blocks, which are grafted outside of the aggregates, stretch along the substrate to facilitate the segregation of B blocks.

By increasing f, we observe that the size of B aggregates decreases and that of A domains increases. The stretching of the bottom A blocks decreases, and at the same time, B domains switch from a continuous layer, to ripples, and finally to dimples. A blocks collapse into domains that are separated from B because the immiscibility and the shape of the aggregates changes from isolated clusters to ripple structures upon increasing f. There is some tendency for A domains to surround B domains because of the solvent preference for the A component, and thus "onion" structures form, as predicted by Zhulina and coworkers by scaling theory.[21]

For B-*b*-A brushes grafted by the ends of the more solvophobic B blocks, there is no lateral structure formation of the top layer at high grafting densities ($\sigma R_{eo}^2 = 12.5$ and 25), but lateral heterogeneity occurs with some voids at sparse grafting ($\sigma R_{eo}^2 = 6.25$), as shown in Figure 11. Collapsed B domains are always pinned to the substrate. A blocks are less insoluble than B blocks, and the surface of B domains is wettable for A blocks. Therefore, A blocks try to cover the B surface homogeneously. When f is small, A blocks are located inside B domains and have the same morphologies as B domains; when f is large, A blocks are long enough and will emerge out of collapsed B domains.

IV. Integral Geometry Analysis

It is already evident from the snapshots of typical system configurations that the morphology of diblock copolymer brushes lacks long-range periodic order. This is in marked contrast with diblock copolymer thin films, which do exhibit rather well-defined order over many molecular extensions, R_{eo}. Previous simulation studies of binary homopolymer brushes indicated that the lack of long-range order can be traced back to the quenched fluctuations of the grafting points, and small fluctuations of the grafting density are amplified by the lateral

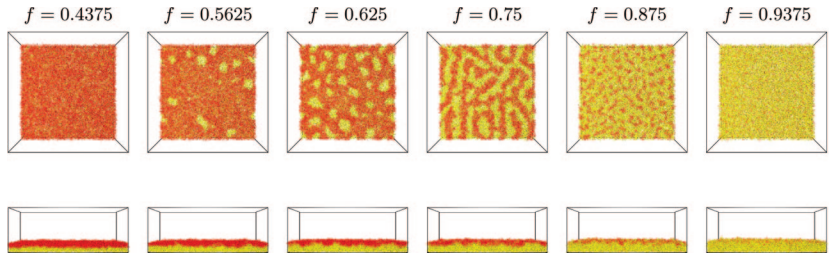

Figure 9. Illustration of morphologies of A-*b*-B diblock brushes in solvent SD for the grafting density $\sigma R_{eo}^2 = 12.5$ and various values of the fraction, *f*, of the A block. The top and side views are presented in the first and second rows, respectively.

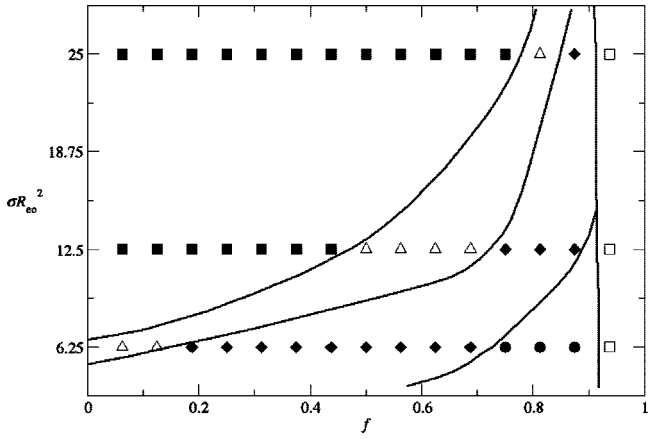

Figure 10. Morphology diagram of A-*b*-B diblock brushes in solvent SD as a function of the fraction, *f*, of A block and the grafting density, σR_{eo}^2: perpendicularly segregated "sandwich" structures (■), perforated layer (△), nearly bicontinuous ripple structures (◆), dimple structures with circular disk domains (●), and structures of unaggregating top blocks (□).

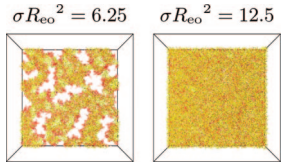

Figure 11. Two typical morphologies of B-*b*-A diblock brushes in solvent SD for $f = 0.5$ and different grafting density.

structure formation inside the binary homopolymer brush.[18] In contrast with a binary homopolymer brush, all grafting points of the diblock copolymer brush belong to the same species, and there are no composition fluctuations of the grafting points. Nevertheless, the irreversible grafting gives rise to quenched density fluctuations, which in a compressible system with asymmetric specific volumes of the different components can couple to the composition. This coupling, in conjunction with the amplification of small fluctuations by the structure formation of the diblock copolymer brush, gives rise to a frozen-in morphology that lacks long-range order.

In experiments, scanning force microscopy (SFM) has extensively been employed in investigating the morphologies of polymer brushes. SFM images of polymer brushes contain a valuable amount of real-space information on surface morphologies, including surface roughness, dominant lateral length scale, domain shape, and connectivity. Routinely, the root-mean-square roughness can be obtained from statistical analysis of height fluctuations, and the dominant lateral length can be determined from 2D Fourier transformation of the SFM images.

The lateral (2D) structure factor for the composition contrast ($\hat{\rho}_B - \hat{\rho}_A$), $S(q)$, extracted from the simulation of an A-*b*-B copolymer brush with grafting density $\sigma R_{eo}^2 = 25$ in solvent

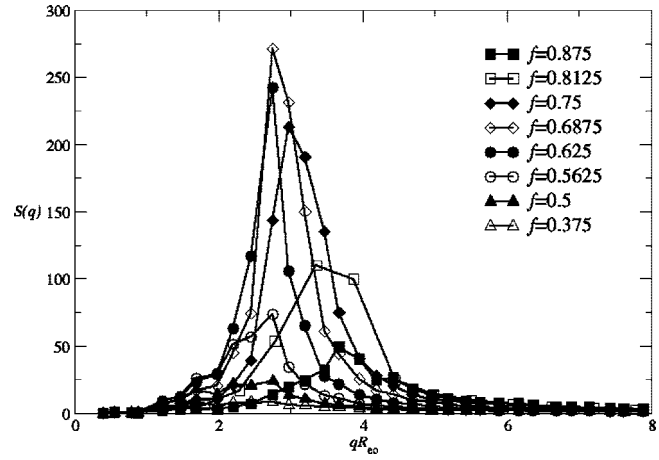

Figure 12. 2D structure factor, $S(q)$, for A-*b*-B diblock brushes in solvent SA for the grafting density $\sigma R_{eo}^2 = 25$ and various values of the fraction, *f*, of A block, as indicated in the key.

SA is presented in Figure 12 as a function of composition, *f*. The structure factor shows a peak, the height of which characterizes the degree of lateral structure formation, and its location is a measure of the dominant lateral length scale, $\lambda = 2\pi/q_{max} \approx 2R_{eo}$. Upon increasing *f*, we observe that lateral structure gradually builds up, becomes most pronounced around $f = 0.6875$, and then decreases for even larger values of *f*. The width of the peak of the structure factor and its location, q_{max}, increases with *f*. The representative snapshots show that the shift in q_{max} mirrors the distance between the collapsed B domains becoming smaller and also their size decreasing. This finding can be rationalized by the scaling of the size of micelle cores in the bulk, $R_{core}/R_{eo} \sim \sqrt[6]{(1-f)\chi N}\sqrt{(1-f)} \sim (1-f)^{2/3}$. Mass conservation dictates that the characteristic distance between micelles is given by $\lambda \sim \sqrt{\rho_{coex} R_{core}^3/[(1-f)\sigma]} \sim \sqrt{1-f}$.

Although the morphology markedly changes with composition, *f*, as can be observed in Figure 1, the variation in $S(q)$ is rather gradual, and it is not obvious how to disentangle the size and shape distribution of the domains from their distance distribution. Whereas the dominant lateral length scale can be clearly identified, the shape of the structure factor cannot be clearly distinguished between ripple- or dimplelike morphologies. This difficulty can be traced back to the lack of long-range periodicity, which is a key characteristic of lateral structures of multicomponent polymer brushes. Techniques from integral geometry analysis may provide a quantification of these disordered morphologies. These techniques have been fruitfully applied to other disordered structures, for example, those occurring in the process of phase separation in the bulk[61] or 2D surface patterns.[62,63]

According to integral geometry, the morphologies in a *D* dimensional space can be completely characterized by $D + 1$ Minkowski functionals. Therefore, in two dimensions, there are three Minkowski functionals that characterize a binary, white-

and-black map: the covered (white) area, S, the length, U, of the boundary between white and black clusters, and the Euler characteristic, χ_E. χ_E is defined as the difference in the number of white clusters and the number of black clusters, and it reflects the connectivity of the clusters. If white clusters are dispersed in a continuous black matrix, then χ_E will be positive. If the white component forms the matrix (e.g., a perforated layer), then χ_E will adopt large negative values. Ripple morphologies are characterized by $\chi_E \approx 0$.

There are a variety of 2D maps that describe the morphology and can be constructed from the multichain configurations of the SCMF simulations. Because the brush is compressible, the composition, $\rho^- \equiv \hat{\rho}_B - \hat{\rho}_A$, and the total density, $\rho^+ \equiv \hat{\rho}_B + \hat{\rho}_A$, characterize the local morphology. To obtain a 2D map, we integrate the two quantities over the coordinate perpendicular to the grafting substrate and obtain $\sum_z \rho^-$ and $\sum_z \rho^+$ as a function of the two lateral coordinates, x and y. The former quantity characterizes the local composition (or the corresponding mechanical properties), whereas the latter quantity describes the height of the brush (or topographical structure). Both characteristics are accessible by SFM experiments. Because there is a large composition difference between domains, the variation in the contrast indicates the size of the domains in the vertical direction, that is, the fraction of the entire brush thickness they occupy. In this way, information about "buried structures" can also be obtained.

For laterally homogeneous structures, the values of the continuous quantity, ξ (being $\sum_z \rho^-$ or $\sum_z \rho^+$), in the original map shows a peak. For laterally segregated structures, ξ typically exhibits a bimodal distribution; each peak around $\xi_<$ and $\xi_>$ corresponds to one of the two physical domains. The values $\xi_<$ and $\xi_>$ provide information about the segregation inside the domains or whether they extend throughout the brush in the vertical direction. To calculate the Minkowski measures, these maps of the continuous quantity, ξ, are converted to binary cluster maps via a threshold procedure; that is, pixels with local variable ξ that is larger or smaller than a given threshold value ξ_t are set to white or black, respectively. From the resulting binary cluster maps, the Minkowski measures can be easily calculated for the different threshold values, ξ_t.[64,65] Rather than characterize a morphology by only the three scalar quantities, S, U, and χ_E, we investigate their dependence on the threshold value, which provides a large amount of information.

The functions $S(\xi_t)$, $U(\xi_t)$, and $\chi_E(\xi_t)$ are presented in Figure 13. For A-*b*-B brushes in solvent SA, we use $\xi = \sum_z \rho^-$, and for A-*b*-B brushes in solvent SC, we employ $\xi = \sum_z \rho^+$ to characterize the lateral structure. The integral area, S, of domains monotonically decreases from its maximal value $S_t = L^2 = (16R_{eo})^2$ to zero upon increasing ξ_t. At both extreme values of ξ_t, the boundary length, U, vanishes, and the Euler characteristic adopts the small absolute value $|\chi_E| = 1$. If the threshold, ξ_t, is very small, then the binary map consists of only a single white cluster. Upon increasing ξ_t, we observe that around $\xi_t \approx \xi_<$, the single cluster of the binary map breaks up, and many black clusters appear. The formation of many small black clusters gives rise to large negative values of χ_E. The threshold value at which this maximum occurs characterizes $\xi_<$, the maximal absolute value of χ_E; however, it does not correspond to simple characteristics of the morphology, but rather it quantifies thermal fluctuations of the quantity ξ inside a domain. Upon further increasing ξ_t, the many small black clusters merge, and χ_E depends less dramatically on the threshold value. This behavior marks the value $\xi_< \ll \xi_t \ll \xi_>$, and the binary cluster map resembles the physical domain distribution. Around $\xi_t \approx (\xi_< + \xi_>)/2$, we find that the number of clusters and the Euler characteristics becomes approximately independent of the threshold value, ξ_t. If the domain morphology is a dimple

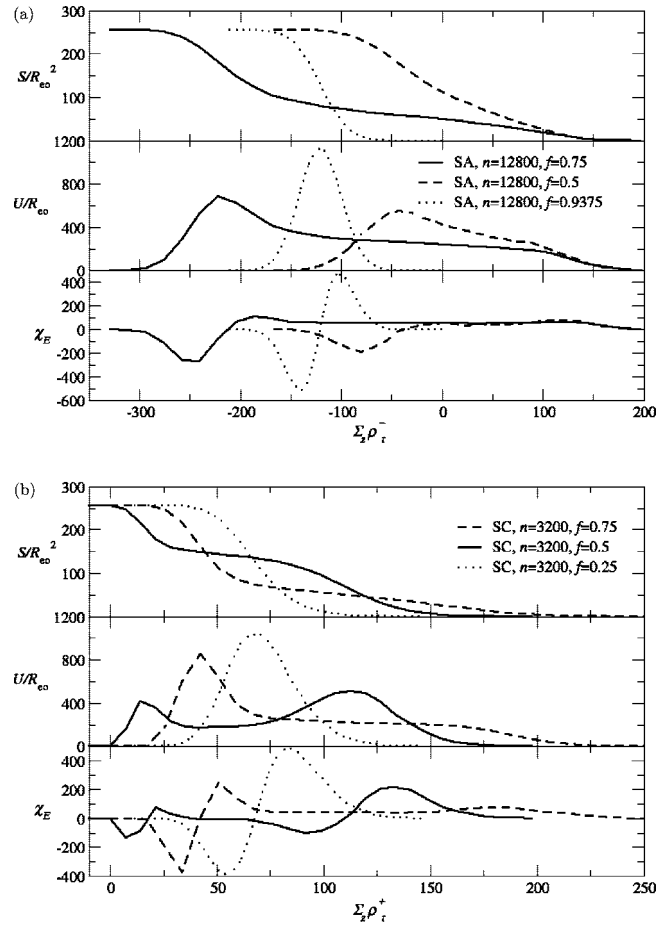

Figure 13. Minkowski measures as a function of the threshold variable. (a) Results for A-*b*-B diblock brushes in solvent SA with the grafting density $\sigma R_{eo}^2 = 50$ using $\sum_z \rho_t^- = \sum_z (\hat{\rho}_B - \hat{\rho}_A)$ as a lateral map. (b) Integral geometry analysis for A-*b*-B diblock brushes in solvent SC with grafting density $\sigma R_{eo}^2 = 12.5$ employing $\sum_z \rho_t^+ = \sum_z (\hat{\rho}_B + \hat{\rho}_A)$ as a lateral map.

structure, where one domain consists of compact patches, whereas the other forms the embedding matrix phase, then the absolute value of the Euler characteristics, $|\chi_E| \approx L^2$, quantifies the number of domains, and its sign identifies which domain forms the matrix. If the domain morphology is a ripple structure, where both domains form elongated domains, then the Euler characteristics will be very small, $\chi_E/L^2 \approx 0$. It is this range of intermediate threshold values that provides information about the lateral morphology of the copolymer brush, and the binary cluster maps yield a representation of the lateral domain structure. Because ξ varies smoothly across the interface between the domains, a change in ξ_t alters the linear extension of a domain by an amount that is comparable to the interface width. As we further increase ξ_t, the white clusters break up. This will occur earlier for white clusters that are ripplelike than for dimplelike aggregates, which have a more uniform distribution of distance between the cluster center and its interface. The small white clusters give rise to positive Euler characteristics, and their proliferation marks the value $\xi_t \approx \xi_>$. For even larger values, the number of white clusters decreases to zero.

If there is a pronounced lateral structure, then the Minkowski measures for $\xi_< \ll \xi_t \ll \xi_>$ provide valuable additional information that complements the lateral structure factor, $S(q)$. In particular, the magnitude of the Euler characteristics quantifies the difference between asymmetric morphologies, where one component forms dimples embedded in a matrix of the other component and more symmetric ripple structures. In Figure 13a and b, we present such an analysis for the morphologies that

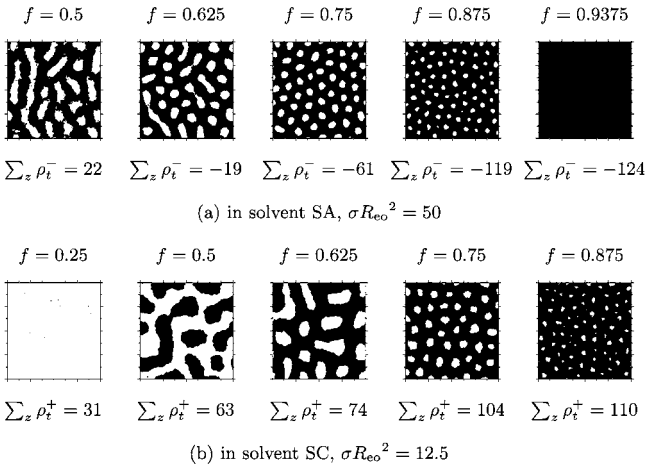

Figure 14. Representative binary cluster maps of A-*b*-B diblock brushes at different values of the fraction, *f*, of the A block (a) in solvent SA with the grafting density $\sigma R_{eo}^2 = 50$ and (b) in solvent SC with the grafting density $\sigma R_{eo}^2 = 12.5$. The representative thresholds, ξ_t, are indicated in the key. For laterally segregated morphologies, $\xi_t \approx (\xi_< + \xi_>)/2$, and for laterally homogeneous morphologies (e.g., $f = 0.9375$ in solvent SA and $f = 0.25$ in solvent SC), the representative thresholds are chosen to eliminate the effect of thermal fluctuations.

an A-*b*-B brush forms in solvents SA and SC, respectively. Snapshots of the morphologies are depicted in Figures 1 and 5, and representative binary cluster maps with $\xi_t \approx (\xi_< + \xi_>)/2$ are shown in Figure 14 as a function of composition, *f*. The comparison of the cluster maps with Figures 1 and 5 demonstrates the consistency between the original morphological images and the corresponding binary maps, which indicates the suitable choice of the threshold value.

In Figure 13a, one clearly notes that the plateau $[\xi_<,\xi_>]$ is much larger for $f = 0.75$ than for $f = 0.5$. This observation correlates with the observation that the amplitude of composition variations is more pronounced for $f = 0.75$, where the domains extend vertically throughout the brush, than for $f = 0.5$, where the lateral structure arises from fluctuations in the A/B interface with small amplitude. In both cases, the plateau value of the Euler characteristics is positive, indicating that white clusters (PS) are embedded in a black matrix (PAA). The plateau value for $f = 0.75$ is $\chi_E \approx 53$, a value that agrees rather well with the number of clusters. For $f = 0.5$, the plateau of the Euler characteristics around $\chi_E \approx 53$ is not so well developed, and there are variations in the threshold value, $\sum_z \rho_t^-$. χ_E is somewhat higher than the number of domains because the shallow composition fluctuations give rise to rather jagged cluster boundaries, and some overhangs are misinterpreted as isolated domains. Therefore, the near-independence of the Minkowski measures from the threshold value, that is, the plateau in Figure 13, is a measure of the degree of lateral structure formation. This becomes evident for large compositional asymmetry, $f = 0.9375$, where no lateral structure is formed (cf. Figure 1). In this case, the Minkowski measures do not exhibit a plateau as a function of the threshold, but the boundary length exhibits a broad peak, and the Euler characteristics have a large negative and a large positive peak. Both indicate the formation of many small clusters in the binary maps due to thermal fluctuations rather than domains. This interpretation agrees with the configuration snapshots.

A similar interpretation holds for the Minkowski measurements of the morphologies in solvent SC, which are presented in of Figure 13b. The plateau is pronounced for $f = 0.75$ and 0.5, but there is no indication of a plateau for $f = 0.25$. In fact, the data for $f = 0.25$ resemble the results for $f = 0.9375$ in solvent SA, indicating that there is no lateral structure. This

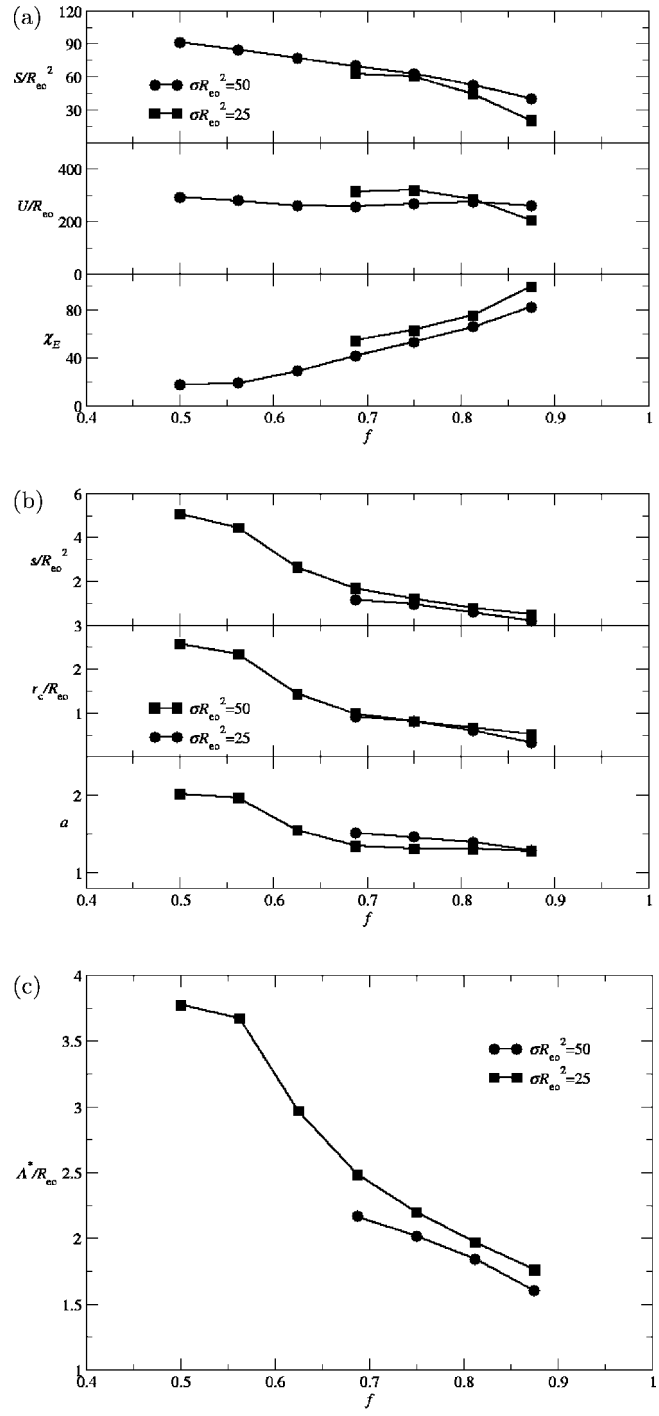

Figure 15. Results of integral geometry analysis on A-*b*-B diblock brushes in solvent SA as a function of the fraction of the A block, *f*. (a) Representative Minkowski measures $\{S,\ U,\ \chi_E\}$. (b) Average area, *s*, mean radius, *r*, and shape parameter, *a*, describing circular feature for individual domains. (c) Lateral dominant length, Λ^*.

interpretation is in agreement with the direct visual inspection of the morphology (cf. Figure 5). The plateau value of the Euler characteristics for $f = 0.75$ is large and positive, indicating that there are many white clusters (i.e., PS domains) embedded in a white matrix (PAA). For $f = 0.5$, however, the Euler characteristics are small, indicating a ripple structure with a similar number of white and black clusters. This interpretation is in agreement with the snapshots.

Figures 15a and 16a show the representative Minkowski measures at the plateau threshold value for A-*b*-B brushes with $\sigma R_{eo}^2 = 50$ in solvent SA and for A-*b*-B brushes with $\sigma R_{eo}^2 =$

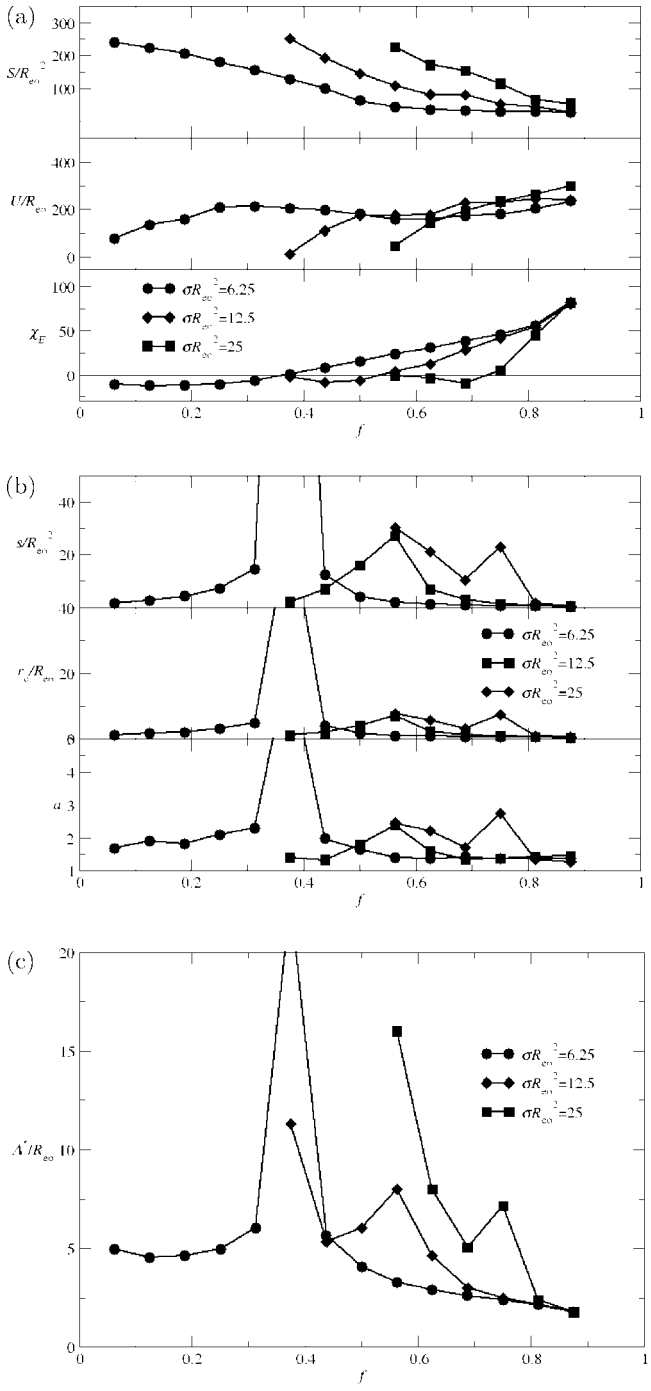

Figure 16. Results of integral geometry analysis on A-*b*-B diblock brushes in solvent SC as a function of the fraction, *f*, of the A block. (a) Representative Minkowski measures {*S*, *U*, χ_E}. (b) Average area, *s*, mean radius, *r*, and shape parameter, *a*, describing circular feature for individual domains. (c) Lateral dominant length, Λ^*.

12.5 in solvent SC, respectively. From the Minkowski measures, *S*, *U*, and χ_E, at the plateau threshold, several quantitative characteristics about domain shapes and sizes can be derived. If one species forms separate domains in a continuous matrix of the other species (i.e., $|\chi_E|$ has a large plateau value), then the average area of a single separate domain can be calculated to be[63]

$$s = \begin{cases} S/\chi_E & \chi_E > 0 \\ (S_t - S)/|\chi_E| & \chi_E > 0 \end{cases} \tag{11}$$

Assuming that the domains are circular in the 2D maps, one obtains for the average domain size

$$r_c = U/(2\pi|\chi_E|) \tag{12}$$

Moreover, we can quantify the shape of a domain by $a \equiv r_c\sqrt{s/\pi}$. For monodisperse circular domains, this shape parameter adopts the value $a_{circ} = 1$. Noncircular domain shape increases *a* because a circle has minimal perimeter for a given area. Figures 15b and 16b present these characteristics of single domain as a function of *f* for block copolymer brushes A-*b*-B in solvent SA and SC, respectively. For block copolymer brushes in solvent SA, by increasing *f* from 0.5 to 0.9, all characteristics, *s*, r_c, and *a*, monotonically decrease. The decrease in the first two quantities indicates that the domain size becomes smaller. Because *a* tends to approach $a_{circ} = 1$, the domains become more circular.

For block copolymer brushes in solvent SC, we observe that with an increases in *f*, *s*, r_c, and *a* first increase and then decrease, which reflects the phase sequence from dimple structures, to ripple structures, to a perforated layer, and to complete coverage. The large values of *s*, r_c, and *a* in the intermediate $f \approx 0.35$ correspond to the ripple structure that is characterized by small values of χ_E. In this case, the Euler characteristics do not quantify the number of compact domains, and the ratios *s*, r_c, and *a* do not possess a simple interpretation as they do for dimple structures.

Additionally, we can characterize a dominant lateral length, Λ^*, by the ratio

$$\Lambda^* = (S_t/|\chi_E|)^{1/2} \tag{13}$$

Figures 15c and 16c show the so-defined dominant lateral length as a function of *f* for A-*b*-B brushes in solvent SA and SC, respectively. Just as for *s*, r_c, and *a*, the estimate, Λ^*, is meaningful for only dimplelike structures. Therefore, no physically meaningful results can be obtained at small χ_E, where the data are strongly affected by the ripple structures; for example, $f \approx 0.35$ at $\sigma R_{eo}^2 = 6.25$, $f \lesssim 0.65$ at $\sigma R_{eo}^2 = 12.5$, and $f \lesssim 0.8$ at $\sigma R_{eo}^2 = 25$ for A-*b*-B diblock brushes in solvent SC, and $f \lesssim 0.7$ for A-*b*-B diblock brushes in solvent SA. For dimple structures at large values of *f* approaching 1, the dominant lateral length monotonically decreases with an increase in *f* for both brushes in SA and SC.

An alternative way to define a family of Minkowski measures for a morphology consists of parallel moving the domain boundary in the representative binary cluster map to obtain a series of new cluster maps. The representative binary cluster map at the threshold $\xi_t \approx (\xi_< + \xi_>)/2$ is described by the boundaries between white and black domains. A family of cluster maps can be obtained by parallel moving the boundaries by an assigned distance, δ. Negative values of δ correspond to eroding white domains. Positive δ values indicate that the white domains has been expanded by a distance, δ, normal to the original boundary; that is, if a pixel in the original map is white (i.e., belongs to a white domain), then all pixels with a distance less than δ are also colored white in the cluster map characterized by the value, δ. With this procedure, a family of parallel boundaries is defined, and the Minkowski measures are calculated for each boundary. The Euler characteristics for an A-*b*-B copolymer brush in solvent SA for the grafting density $\sigma R_{eo}^2 = 50$ are shown in Figure 17 as a function of δ. The values for $\xi_t \approx (\xi_< + \xi_>)/2$ of the threshold method and $\delta = 0$ of the parallel boundary method agree. The advantage of the latter procedure is its insensitivity to thermal fluctuations and the concomitant elimination of the proliferation of clusters in the threshold method. Moreover, the parallel displacement, δ, has a simple geometrical meaning and provides rather direct information about the size of domains. Unlike the threshold method, however, the degree of segregation cannot be quantified because this information is already lost in the original cluster map.

If $-\delta$ exceeds the extension of white domains, the cluster map will be composed of a single black cluster. Likewise, if δ

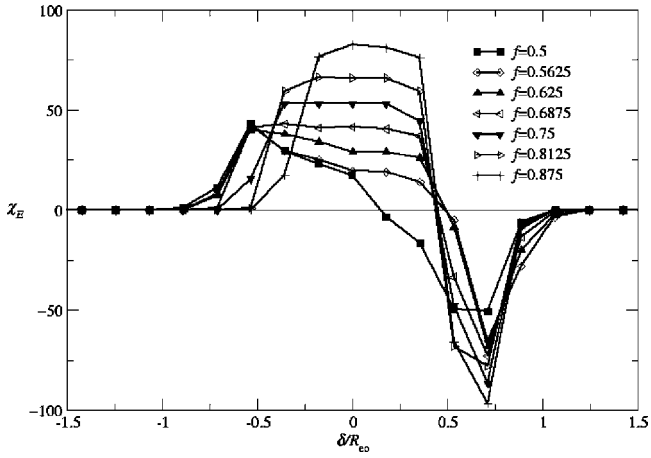

Figure 17. Euler characteristics, χ_E, of the morphologies of A-*b*-B diblock brushes in solvent SA for the grafting density $\sigma R_{eo}^2 = 50$ as a function of the expanding distance, δ, using the parallel boundary method.

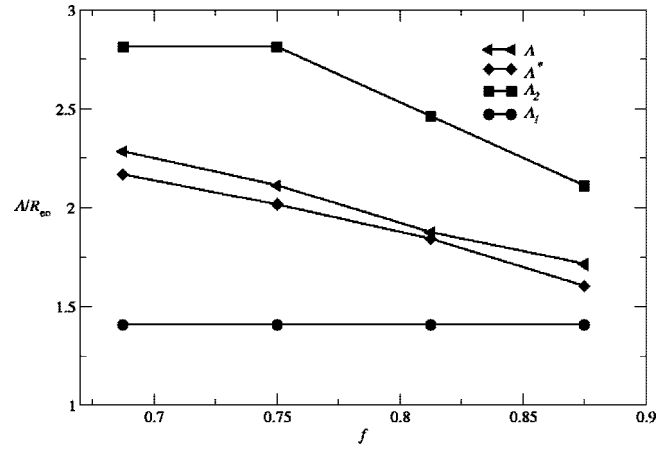

Figure 18. Dominant lateral length of A-*b*-B diblock brushes in solvent SA for the grafting density $\sigma R_{eo}^2 = 50$ as a function of the fraction of the A block. Λ is determined from the peak of the 2D structure factor shown in Figure 12, Λ^* is determined from the representative Euler characteristics in Figure 15a using eq 13, and Λ_1 and Λ_2 are determined using parallel boundary technique, as illustrated in Figure 17.

exceeds the extension of black clusters in the original map (white domains), the cluster map will consist of a single white cluster. Between these two limits, S increases monotonically with increasing δ, and U exhibits a peak. From the Euler characteristics in Figure 17 for an A-*b*-B diblock brush in SA for $\sigma R_{eo}^2 = 50$ for $0.3 \lesssim f \lesssim 0.65$, a lateral ripple structure emerges, and its segregation increases with f. For $|\delta| \ll R_{eo}$, the numbers of white and black ripples are roughly equal, and the Euler characteristics is small. Upon decreasing δ, one erodes white domains, and if $-\delta$ is comparable to the width of the elongated white domains, then they will break up into many smaller clusters. This is signaled by a maximum in the Euler characteristics. Upon increasing δ from the original domain map, one erodes black clusters, and the location of the maxima of $-\chi_E$ quantifies the typical width of the elongated black clusters. Therefore, a ripple structure is characterized by a linear decrease in the Euler characteristics around $\delta \approx 0$, and the location of the maxima of its absolute value $|\chi_E|$ characterizes the width of the ripples.

Around $f \simeq 0.65$, the morphology gradually changes from ripplelike to dimplelike. Upon approaching the highest value, $f \approx 0.9$, the dimples decrease in size, and eventually, a disordered structure (beyond $f \approx 0.9$) is formed. The dependence of the Euler characteristics on δ for a dimple structure is very different from that for a ripple structure. The absolute value of the Euler characteristics is large at $\delta \approx 0$ because it is proportional to the number of dimples. Its value hardly changes with δ around $\delta \approx 0$ because a slight increase or decrease in the dimple diameter does not affect the number. Only if $\delta \lesssim -D/2$, with D being the diameter of the circular white domains, will white clusters disappear and χ_E decrease. Therefore, the decrease in χ_E at negative δ provides information about the dimple diameter. In the opposite limit, $\delta > 0$, the white clusters expand, and they will begin to merge if $\delta > \Delta/2$, with Δ being the closest distance between boundaries of the original domain map across the black matrix. The merger of white clusters goes along with a decrease in χ_E from its maximal value around $\delta \approx 0$. If we further increase δ, $\delta \gg \Delta/2$, then the white clusters will start to percolate and form the matrix. At this point, χ_E changes its sign and becomes negative. Eventually, all remaining white clusters disappear, and χ_E approaches the value -1.

Several characteristic length scales can be extracted from the Minkowski measures as a function of the parallel boundaries. $\Lambda_1/2$ is the distance between the minimum and the maximum of χ_E. For an ideal ripple structure, that is, a periodic stripe pattern, Λ_1 corresponds to the periodicity (i.e., the thickness of white and black stripes). Alternatively, one can consider the distance $\Lambda_2/2$ between the rise of χ_E at negative values of δ and the minimum χ_E for $\delta > 0$. In an ideal, regular array of disklike domains, this quantity characterizes the distance between the centers of the discs. In Figure 18, for A-*b*-B diblock brushes in solvent SA for the grafting density $\sigma R_{eo}^2 = 50$, these two quantities, Λ_1 and Λ_2, are compared with Λ determined from the peak of the 2D structure factor and Λ^* determined from the representative Euler characteristics using eq 13. The result, Λ^*, obtained from the structure factor is in good agreement with Λ obtained from structure factors, and both values, Λ and Λ^*, are bracketed by Λ_1 and Λ_2.

V. Discussion

We have presented a systematic investigation of structure formation in copolymer brushes as a function of the selectivity of the surrounding solvent, the grafting density, and the compositional asymmetry. Whereas our coarse-grained model with soft interactions is inspired by a specific experimental system, we expect that the qualitative behavior is shared by a broad class of stimuli-responsive copolymer brushes. A rich variety of structures with varying degrees of perpendicular and lateral segregation has been observed, and the morphologies have been compared with theoretical predictions, other simulation studies, and experiments.

Most notable is the fact that lateral structures lack long-range periodicity. Because our coarse-grained model with soft interactions can be simulated very efficiently, this finding cannot be traced back to failure to equilibrate the morphology, but it is related to fluctuations in the grafting points. Through the coupling of density to composition fluctuations, small fluctuations in the grafting density are amplified by the structure formation in the brush and dictate the location of the domains. This effect deserves further analysis, which will be presented elsewhere. Here we note that this lack of long-range order is also born out by experiments. Because of the lack of long-range order, the changes in different morphologies are not thermodynamic transitions but rather gradual crossovers where the characteristics of the morphology continuously change with the control parameter (e.g., composition or grafting density).

Because of the lack of periodicity, the structure factor of composition or density/height fluctuations provides a very crude quantification of the lateral structure. Only the dominant lateral length scale can be identified, but different domain morpholo-

gies, for example, dimple or ripple structures, are difficult to distinguish. We have proposed two techniques, threshold method and parallel boundary technique, to generate a family of binary 2D maps from the 2D map of the morphology and have analyzed them via calculating Minkowski functions. These quantities are well-suited to characterize disordered morphologies and allow for a clear distinction between dimple and ripple structures. The integral analysis may provide a suitable means for quantifying these gradual morphological changes in SFM experiments and for complementing the characterization by the structure factor. We hope that experimental data will be analyzed in terms of Minkowski measures and allow for a quantitative comparison with simulation data.

Acknowledgment. We thank K. Hinrichs, I. Luzinov, S. Minko, and M. Stamm for stimulating discussions. Financial support by the DFG-NSF Materials World Network program under grant Mu 1674/9 is gratefully acknowledged. Ample computing time has been provided by the GWDG Göttingen, the HLRN Hannover, and the JSC Jülich.

References and Notes

(1) Pincus, P. *Macromolecules* **1991**, *24*, 2912.
(2) Galaev, I. Y.; Mattiasson, B. *Trends Biotechnol.* **1999**, *17*, 335.
(3) Leger, L.; Raphael, E.; Hervet, H. *Polym. Confined Environ.* **1999**, *138*, 185.
(4) Mansky, P.; Liu, Y.; Huang, E.; Russel, T. P.; Hawker, C. J. *Science* **1997**, *275*, 1458.
(5) Zhao, B.; Brittain, W. J. *Prog. Polym. Sci.* **2000**, *25*, 677.
(6) Luzinov, I.; Minko, S.; Tsukruk, V. V. *Prog. Polym. Sci.* **2004**, *29*, 635.
(7) Brittain, W. J.; Minko, S. *J. Polym. Sci., Part A: Polym. Chem.* **2007**, *45*, 3505.
(8) Minko, S.; Usov, D.; Goreshnik, E.; Stamm, M. *Macromol. Rapid. Commun.* **2001**, *22*, 206.
(9) Sidorenko, A.; Minko, S.; Schenk-Meuser, K.; Duschner, H.; Stamm, M. *Langmuir* **1999**, *15*, 8349.
(10) Zhao, B.; Brittain, W. J.; Zhou, W.; Cheng, S. Z. D. *J. Am. Chem. Soc.* **2000**, *122*, 2407.
(11) Zhao, B.; Brittain, W. J.; Zhou, W.; Cheng, S. Z. D. *Macromolecules* **2000**, *33*, 8821.
(12) Minko, S.; Müller, M.; Motornov, M.; Nitschke, M.; Grundke, K.; Stamm, M. *J. Am. Soc. Chem.* **2003**, *125*, 3896.
(13) Hoy, O. Ph.D. Thesis, Clemson University, **2008**.
(14) Santer (Prokhorova), S.; Rühe, J. *Polymer* **2004**, *45*, 8279.
(15) Santer, S.; Kopyshev, A.; Donges, J.; Yang, H.-K.; Rühe, J. *Adv. Mater.* **2006**, *18*, 2359.
(16) Santer, S.; Kopyshev, A.; Donges, J.; Yang, H.-K.; Rühe, J. *Langmuir* **2006**, *22*, 4660.
(17) Santer, S.; Kopyshev, A.; Donges, J.; Rühe, J.; Jiang, X.; Zhao, B.; Müller, M. *Langmuir* **2007**, *23*, 279.
(18) Wenning, L.; Müller, M.; Binder, K. *Europhys. Lett.* **2005**, *71*, 639.
(19) Singh, C.; Balazs, A. C. *Macromolecules* **1996**, *29*, 8904.
(20) Zhulina, E.; Singh, C.; Balazs, A. C. *Macromolecules* **1996**, *29*, 8254.
(21) Zhulina, E.; Singh, C.; Balazs, A. C. *Macromolecules* **1996**, *29*, 6338.
(22) Balazs, A. C.; Singh, C.; Zhulina, E.; Chern, S.-S.; Lyatskaya, Y.; Pickett, G. T. *Prog. Surf. Sci.* **1997**, *55*, 181.
(23) Singh, C.; Pickett, G. T.; Zhulina, E.; Balazs, A. C. *J. Phys. Chem. B* **1997**, *101*, 10614.
(24) Zhulina, E.; Singh, C.; Balazs, A. C. *J. Chem. Phys.* **1998**, *108*, 1175.
(25) Singh, C.; Pickett, G. T.; Balazs, A. C. *Macromolecules* **1996**, *29*, 7559.
(26) Singh, C.; Zhulina, E.; Gersappe, D.; Pickett, G. T.; Balazs, A. C. *Macromolecules* **1996**, *29*, 7637.
(27) Singh, C.; Balazs, A. C. *J. Chem. Phys.* **1996**, *105*, 706.
(28) Brown, G.; Chakrabarti, A.; Marko, J. F. *Macromolecules* **1995**, *28*, 7817.
(29) Yin, Y.; Sun, P.; Li, B.; Chen, T.; Jin, Q.; Ding, D.; Shi, A.-C. *Macromolecules* **2007**, *40*, 5161.
(30) Romiszowski, P.; Sikorski, A. *J. Phys.: Condens. Matter* **2007**, *19*, 205137.
(31) Müller, M.; MacDowell, L. G.; Virnau, P.; Binder, K. *J. Chem. Phys.* **2002**, *117*, 5480.
(32) Van Konynenburg, P. H.; Scott, R. L. *Philos. Trans. R. Soc. Lomdon, Ser. A* **1980**, *298*, 495.
(33) Note that ρ is a dimensionless quantity that does not make reference to the number of effective interaction centers, N, used to discretize the chain contour. Therefore, it is an invariant of our coarse-grained model that would not change if we chose a different discretization and can be directly compared to experiments. By the same token, the coefficients of the nonbonded interaction free energy function, eq 2, are also invariants. For instance, the second-order term, v_{AA}, is related to the segmental virial coefficient, $\tilde{v}_{AA}$, via $v_{AA} = (\tilde{v}_{AA}N^2)/(R_{co}^3)$; that is, v_{AA} is the Fixmann parameter that describes the strength of the excluded volume interaction.
(34) *Polymer Handbook*, 4th ed.; Brandrup, J., Immergut, E. H., Grulke, E. A., Eds.; Wiley-Interscience: New York, 1999.
(35) Yu, X.; Wang, X.; Wang, H.; Li, X.; Gao, J. *QSAR Comb. Sci.* **2006**, *25*, 156.
(36) Usually, Flory−Huggins parameters can be calculated from the solubility parameters, and those parameters between polymers and solvent SB (MEK) are calculated using this method. However, Flory−Huggins parameters calculated this way cannot reflect hydrogen bond and electrostatic interaction, which are important in solvent SA (DMF), SC, and SD (water). Instead of considering these complicated interactions in a sophisticated model, for simplicity, some estimated Flory−Huggins parameters are adopted to reflect the solvent quality.
(37) Müller, M.; Daoulas, K. Ch. *J. Chem. Phys.* **2008**, *128*, 024903.
(38) Müller, M.; Daoulas, K. Ch. *J. Chem. Phys.* **2008**, *129*, 164906.
(39) Detcheverry, F. A.; Kang, H.; Daoulas, K. Ch.; Müller, M.; Nealey, P. F.; de Pablo, J. J. *Macromolecules* **2008**, *41*, 2759.
(40) Dawson, K. A.; March, N. H. *Phys. Lett. A* **1983**, *96*, 460.
(41) Eastwood, J. W.; Hockney, R. W.; Lawrence, D. N. *Comput. Phys. Commun.* **1980**, *19*, 215.
(42) Deserno, M.; Holm, C. *J. Chem. Phys.* **1998**, *109*, 7678.
(43) Müller, M.; Smith, G. D. *J. Polym. Sci., Part B: Polym. Phys.* **2005**, *43*, 934.
(44) Daoulas, K. Ch.; Müller, M.; de Pablo, J. J.; Nealey, P. F.; Smith, G. D. *Soft Matter* **2006**, *2*, 573.
(45) Daoulas, K. Ch.; Müller, M. *J. Chem. Phys.* **2006**, *125*, 184904.
(46) Allen, M. P.; Tildesley, D. J. *Computer Simulation of Liquids*; Clarendon Press: Oxford, England, 1987.
(47) Rossky, P. J.; Doll, J. D.; Friedman, H. L. *J. Chem. Phys.* **1978**, *69*, 4628.
(48) de Gennes, P.-G. *Scaling Concepts in Polymer Physics*; Cornell University Press: Ithaca, NY, 1979.
(49) Cavallo, A.; Müller, M.; Binder, K. *Macromolecules* **2008**, *41*, 4937.
(50) Xiong, H.; Zheng, J. X.; Van Horn, R. M.; Jeong, K.-U.; Quirk, R. P.; Lotz, B.; Thomas, E. L.; Brittain, W. J.; Cheng, S. Z. D. *Polymer* **2007**, *48*, 3732.
(51) Huang, W. H.; Luo, C. X.; Zhang, J. L.; Yu, K.; Han, Y. C. *Macromolecules* **2007**, *40*, 8022.
(52) Boyes, S. G.; Brittain, W. J.; Weng, X.; Cheng, S. Z. D. *Macromolecules* **2002**, *32*, 1424.
(53) Huang, W.; Kim, J. B.; Baker, G. L.; Bruening, M. L. *Nanotechnology* **2003**, *14*, 1075.
(54) Kong, B.; Lee, J. K.; Choi, I. S. *Langmuir* **2007**, *23*, 6761.
(55) Xu, C.; Wu, T.; Drain, C. M.; Batteas, J. D.; Fasolka, M. J.; Beers, K. L. *Macromolecules* **2004**, *39*, 3359.
(56) Tomlinson, M. R.; Genzer, J. *Langmuir* **2005**, *21*, 11552.
(57) Semenov, A. N. *Sov. Phys. JETP* **1985**, *61*, 733.
(58) Williams, D. R. M. *J. Phys. II* **1993**, *3*, 1313.
(59) Yeung, C.; Balazs, A. C.; Jasnow, D. *Macromolecules* **1993**, *26*, 1914.
(60) Lai, P.-Y.; Binder, K. *J. Chem. Phys.* **1992**, *97*, 586.
(61) Mao, Y.; McLeish, T. C. B.; Teixeira, P. I. C.; Read, D. J. *Eur. Phys. J. E* **2001**, *6*, 69.
(62) Gutmann, J. S.; Muller-Buschbaum, P.; Stamm, M. *Faraday Discuss.* **1999**, *112*, 285.
(63) Raczkowska, J.; Rysz, J.; Budkowski, A.; Lekki, J.; Lekka, M.; Bernasik, A.; Kowalski, K.; Czuba, P. *Macromolecules* **2003**, *36*, 2419.
(64) Michielsen, K.; De Raedt, H. *Comput. Phys. Commun.* **2000**, *132*, 94.
(65) Legland, D.; Ki eu, K.; Devaux, M.-F. *Image Anal. Stereol.* **2007**, *26*, 83.

MA8026047